GEOPHYSICS, VOL. 82, NO. 6 (NOVEMBER-DECEMBER 2017); P. Q53–Q66, 8 FIGS.
10.1190/GEO2017-0166.1

Target-enclosed seismic imaging

Joost van der Neut[1], Matteo Ravasi[2], Yi Liu[3], and Ivan Vasconcelos[4]

ABSTRACT

Seismic reflection data can be redatumed to a specified boundary in the subsurface by solving an inverse (or multidimensional deconvolution) problem. The redatumed data can be interpreted as an extended image of the subsurface at the redatuming boundary, depending on the subsurface offset and time. We retrieve target-enclosed extended images by using two redatuming boundaries, which are selected above and below a specified target volume. As input, we require the upgoing and downgoing wavefields at both redatuming boundaries due to impulsive sources at the earth's surface. These wavefields can be obtained from actual measurements in the subsurface, they can be numerically modeled, or they can be retrieved by solving a multidimensional Marchenko equation. As output, we retrieved virtual reflection and transmission responses as if sources and receivers were located at the two target-enclosing boundaries. These data contain all orders of reflections inside the target volume but exclude all interactions with the part of the medium outside this volume. The retrieved reflection responses can be used to image the target volume from above or from below. We found that the images from above and below are similar (given that the Marchenko equation is used for wavefield retrieval). If a model with sharp boundaries in the target volume is available, the redatumed data can also be used for two-sided imaging, where the retrieved reflection and transmission responses are exploited. Because multiple reflections are used by this strategy, seismic resolution can be improved significantly. Because target-enclosed extended images are independent on the part of the medium outside the target volume, our methodology is also beneficial to reduce the computational burden of localized inversion, which can now be applied inside the target volume only, without suffering from interactions with other parts of the medium.

INTRODUCTION

We start with a short introduction. This is followed by an outline and a short review of reciprocity theorems, which play an important role throughout the paper.

Motivation

Seismic redatuming uses reflection measurements at the earth's surface to obtain a virtual data set, as if sources and receivers had been installed inside the subsurface (Berryhill, 1984). The redatumed data, which are a function of subsurface offset and time, can be interpreted as an extended image of the subsurface (Vasconcelos et al., 2010). A conventional image can be computed by evaluating the extended image at zero time and zero subsurface offset. This methodology can be applied for various purposes, including structural reflection imaging (Claerbout, 1971; Berkhout, 1980), migration velocity analysis (Sava and Vasconcelos, 2010; Mildner et al., 2017), and more quantitative subsurface characterization (de Bruin et al., 1990; Ordoñez et al., 2016; Thomson et al., 2016).

Redatuming can be achieved by crosscorrelating the acquired reflection data with a wavefield extrapolator, which is typically computed in a smooth subsurface model. It is well-known that multiple reflections in the medium are not addressed by this procedure, which can lead to the emergence of spurious arrivals in the redatumed data space (Malcolm et al., 2007). In theory, more accurate results can be achieved if propagators are computed in the physical medium (Bakulin and Calvert, 2006; Schuster and Zhou, 2006), and if upgoing and downgoing wavefields are separated (Mehta et al., 2007). However, to eliminate all spurious events from redatumed gathers, reflection data should be acquired along a closed boundary

Manuscript received by the Editor 14 March 2017; revised manuscript received 15 May 2017; published ahead of production 05 July 2017; published online 21 August 2017.
[1]Delft University of Technology, Department of Geosciences, Delft, the Netherlands. E-mail: j.r.vanderneut@tudelft.nl.
[2]Formerly University of Edinburgh, School of GeoSciences, Edinburgh, UK; presently Statoil ASA, Bergen, Norway. E-mail: mrava@statoil.com.
[3]Norwegian University of Science and Technology, Department of Petroleum Engineering and Applied Geophysics, Trondheim, Norway. E-mail: yi.liu@ntnu.no.
[4]Formerly Schlumberger Gould Research, Cambridge, UK; presently Department of Earth Sciences, Utrecht, the Netherlands. E-mail: i.vasconcelos@uu.nl.

surrounding the new subsurface datum (Snieder et al., 2006). Unfortunately, such data cannot typically be acquired in conventional seismic surveys. To overcome these limitations, one may apply redatuming by inversion (Xue and Schuster, 2008; Wapenaar and van der Neut, 2010; Vasconcelos and Rickett, 2013; Aldawood et al., 2015), which can be interpreted as a multidimensional deconvolution process. As a consequence of deconvolution, the redatumed data contain no interaction with the part of the medium above the redatuming level. This special property of multidimensional deconvolution has been exploited before, for instance, to remove interactions from the air-water interface in marine seismic data (Amundsen, 2001; van Groenestijn and Verschuur, 2009; Lin and Herrmann, 2013) or from a complex overburden in downhole data (van der Neut et al., 2016).

To implement redatuming through a heterogeneous overburden, in practice, we require knowledge of the Green's functions in the physical subsurface. This approach demands a highly detailed subsurface model or actual measurements in the subsurface, for instance, by placing receivers in boreholes. Because the recorded downhole waveforms can be directly related to the required Green's functions, seismic redatuming can be realized without a subsurface model, either by crosscorrelation (Bakulin and Calvert, 2006; Mehta et al., 2007) or by inversion (van der Neut et al., 2016).

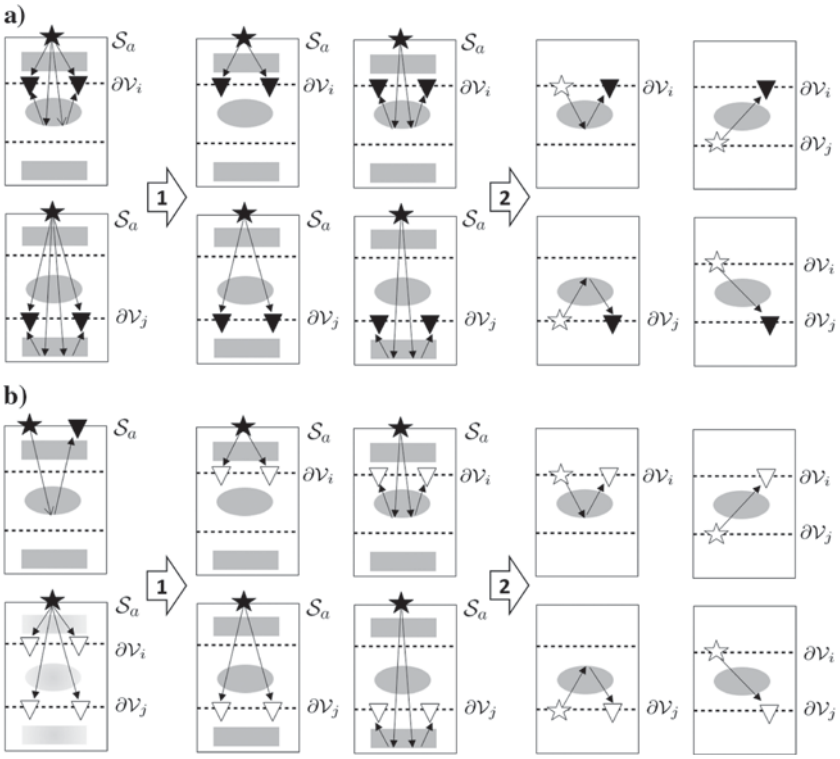

Figure 1. (a) Target-enclosed redatuming when data are physically recorded at two boundaries $\partial\mathcal{V}_i$ and $\partial\mathcal{V}_j$. In step (1), the data are decomposed into its upgoing and downgoing constituents. In step (2), the sources are redatumed. (b) Target-enclosed redatuming when data are recorded at the acquisition boundary $\mathcal{S}_a$ (in the lower-left corner, we show the smooth background model). In step (1), upgoing and downgoing wavefields are retrieved, for instance, by solving the multidimensional Marchenko equation. In step (2), the sources are redatumed. Black stars and triangles represent physical sources and receivers. White stars and triangles represent virtual sources and receivers. Note that the redatumed data are defined in a reference medium, which is reflection-free above $\partial\mathcal{V}_i$ and below $\partial\mathcal{V}_j$, but identical to the physical medium in between these boundaries.

The required wavefields may also be computed by evaluating an inverse scattering series (Weglein et al., 2003) or a Bremmer series (Malcolm et al., 2009; Davydenko and Verschuur, 2016). Alternatively, we can estimate the required Green's functions directly from the reflection data that are acquired at the earth's surface by solving a multidimensional Marchenko equation (Broggini et al., 2012; Slob et al., 2014; Wapenaar et al., 2014; da Costa Filho et al., 2015; Singh et al., 2015). Internal multiples are effectively accounted for by this methodology even though it only requires a smooth subsurface model (Behura et al., 2014; Broggini et al., 2014; Mildner et al., 2017).

By solving the multidimensional Marchenko equation, all primary and multiple reflections at a given boundary in the subsurface can be retrieved, bypassing the need to resolve the overburden in detail. Hence, deep primary reflections from below the overburden can be imaged, without suffering from the disturbing effect of overburden-related multiples (Wapenaar et al., 2014). It can be shown that linear imaging of the redatumed data is equivalent to the imaging of primaries (Wapenaar et al., 2017). Hence, Marchenko imaging can also be interpreted as an internal multiple elimination process (Meles et al., 2015; van der Neut and Wapenaar, 2016; da Costa Filho et al., 2017). However, it has also been recently shown that novel imaging conditions can be derived for multiply reflected waves, given that a detailed model of the subsurface is available (Halliday and Curtis, 2010; Fleury and Vasconcelos, 2012; Ravasi et al., 2014, 2015b). To evaluate these imaging conditions, we require reflection and transmission responses from two boundaries that enclose the target volume. Unfortunately, such data are generally not available. To facilitate the implementation of these imaging conditions in practice, we present a methodology by which these responses, which we refer to as target-enclosed extended images, can be retrieved from seismic reflection data at a single acquisition boundary. As we demonstrate with a synthetic example, this methodology allows us to improve seismic resolution in the target volume, given that a model with sharp boundaries in that volume is available.

Outline

The goal of this paper is to present for the first time how target-enclosed extended images can be obtained and how they can be used for imaging a target volume. As input, we require upgoing and downgoing Green's functions, with sources at the acquisition boundary and receivers at two redatuming boundaries $\partial\mathcal{V}_i$ and $\partial\mathcal{V}_j$, located above and below a selected target volume $\mathcal{V}$ in the subsurface, respectively. These Green's functions can be computed in a detailed subsurface model or they can be directly measured in boreholes. In the latter case, the recorded waveforms should be decomposed into their upgoing and downgoing components (Mehta et al., 2007; van der Neut et al., 2016), as illustrated in Figure 1a. The required Green's functions can also be computed by solving a multidimensional Marchenko equa-

tion (Wapenaar et al., 2014), as shown in Figure 1b. This approach requires seismic data to be recorded at acquisition boundary $\mathcal{S}_a$ and a macro model of the propagation velocity.

In Figure 1a and 1b, we transform the Green's functions (which are either measured or retrieved) into a virtual data set, as if sources and receivers had been installed at $\partial\mathcal{V}_i$ and $\partial\mathcal{V}_j$. These virtual data contain (1) the reflection response of the target volume from the upper boundary, (2) the reflection response of the target volume from the lower boundary, and (3) the transmission response from the upper to the lower boundary. To retrieve these responses, we solve an inverse problem, which is derived from reciprocity theorems of the convolution and the correlation type. We describe this methodology in the section "Target-enclosed redatuming with Green's functions." In the next section, "Target-enclosed redatuming with focusing functions," we present an alternative approach that is based on focusing functions, rather than on the Green's functions. Akin to the Green's functions, these focusing functions can also be retrieved by solving a multidimensional Marchenko equation. In the "Examples" section, the methodology is demonstrated on 2D synthetic data and used to image a target volume from above and from below. In the "Discussion" section, we argue whether to use the Green's functions or the focusing functions for redatuming. We also compare imaging from above to imaging from below. Finally, we discuss how the retrieved reflection responses and the retrieved transmission response can be used to improve seismic resolution, in case a velocity model with sharp boundaries in the target volume is available.

Review

Throughout the paper, we consider wave propagation in a lossless acoustic medium, which is defined by the density $\varrho(\mathbf{x})$ and the velocity $c(\mathbf{x})$, where $\mathbf{x} = (x, y, z)$ is a spatial Cartesian coordinate system. Acoustic pressure fields are described in the frequency domain as $p(\mathbf{x}, \omega)$, where ω is the angular frequency. These fields obey a (modified) Helmholtz equation, which is given by (Wapenaar and Grimbergen, 1996)

$$(\varrho\partial_z(\varrho^{-1}\partial_z\,\cdot) + \mathcal{H}_2)p = -j\omega\varrho q, \tag{1}$$

where $\partial_z = (\partial/\partial z)$, q is a volume injection rate density source, and j is the imaginary unit. The (modified) Helmholtz operator $\mathcal{H}_2$ is defined as

$$\mathcal{H}_2 = \frac{\omega^2}{c^2} + \varrho\partial_x(\varrho^{-1}\partial_x\,\cdot) + \varrho\partial_y(\varrho^{-1}\partial_y\,\cdot), \tag{2}$$

where $\partial_x = (\partial/\partial x)$ and $\partial_y = (\partial/\partial y)$. If medium properties are constant or vary only smoothly at a depth level, the pressure field can be locally decomposed into its downgoing components p^+ and upgoing components p^-, where $p = p^+ + p^-$. These decomposed quantities obey the one-way wave equation (Wapenaar and Grimbergen, 1996):

$$\partial_z\begin{pmatrix} p^+ \\ p^- \end{pmatrix} = -j\mathcal{H}_1\begin{pmatrix} p^+ \\ -p^- \end{pmatrix}, \tag{3}$$

where $\mathcal{H}_1$ is a square-root operator that obeys $\mathcal{H}_2 = \mathcal{H}_1\mathcal{H}_1$ (Grimbergen et al., 1998). In Appendix A, we show how this operator can be computed numerically. Reciprocity theorems can be derived between decomposed fields in state A (indicated by subscript A) and decomposed fields in state B (indicated by subscript B). For this purpose, we define a cylindrical volume $\mathcal{V}$ in the subsurface, which is bounded by two infinite horizontal boundaries $\partial\mathcal{V}_i$ at z_i at the top and $\partial\mathcal{V}_j$ at z_j at the bottom. The medium properties in states A and B are identical inside $\mathcal{V}$ but can be arbitrarily chosen outside this volume. Further, we assume that no sources exist inside the volume. We distinguish the reciprocity theorem of the convolution type (Wapenaar et al., 2014)

$$\int_{\partial\mathcal{V}_i} dxdy\varrho^{-1}(p_A^+(\partial_z p_B^-) + p_A^-(\partial_z p_B^+)) = \int_{\partial\mathcal{V}_j} dxdy\varrho^{-1}(p_A^+(\partial_z p_B^-) + p_A^-(\partial_z p_B^+)), \tag{4}$$

and the reciprocity theorem of the correlation type (Wapenaar et al., 2014)

$$\int_{\partial\mathcal{V}_i} dxdy\varrho^{-1}(p_A^{+*}(\partial_z p_B^+) + p_A^{-*}(\partial_z p_B^-)) = \int_{\partial\mathcal{V}_j} dxdy\varrho^{-1}(p_A^{+*}(\partial_z p_B^+) + p_A^{-*}(\partial_z p_B^-)), \tag{5}$$

where superscript $*$ denotes complex conjugation.

TARGET-ENCLOSED REDATUMING WITH GREEN'S FUNCTIONS

In this section, we derive representations for target-enclosed redatuming with Green's functions. We start with a definition of Green's functions and their properties. Then, we derive representations for Green's functions at the upper boundary $\partial\mathcal{V}_i$ due to impulsive sources at the earth's surface. We do the same for Green's functions at the lower boundary $\partial\mathcal{V}_j$. Finally, we show how target-enclosed extended images can be retrieved by inverting these representations.

Green's functions

The Green's function $G(\mathbf{x}, \mathbf{x}_s, \omega)$ is defined as the pressure field $p(\mathbf{x}, \omega)$ due to an impulsive source at location $\mathbf{x}_s = (x_s, y_s, z_s)$. For notational convenience, we omit the dependence of the Green's function on ω in the following derivation. The Green's function obeys wave equation 1, with the following source term:

$$q = \delta(x - x_s)\delta(y - y_s)\delta(z - z_s), \tag{6}$$

where $\delta(x)$ is a Dirac-delta function. If the half-space above z_s is reflection-free, the following limit can be derived for the vertical derivative of the downgoing Green's function (Wapenaar et al., 2014):

$$\lim_{z\to z_{s+}} \partial_z G^+(\mathbf{x}, \mathbf{x}_s) = -\frac{j\omega\varrho}{2}\delta(x - x_s)\delta(y - y_s), \tag{7}$$

where z_{s+} is z_s in the limit from below. Because $\lim_{z\to z_{s-}} \partial_z G^+(\mathbf{x}, \mathbf{x}_s) = 0$ (where z_{s-} is z_s in the limit from above), the downgoing Green's function is discontinuous at the source location. Similarly, if the half-space below z_s is reflection-free, we find the following limit for the vertical derivative of the upgoing Green's function:

$$\lim_{z\to z_{s-}} \partial_z G^-(\mathbf{x},\mathbf{x}_s) = \frac{j\omega\varrho}{2}\delta(x-x_s)\delta(y-y_s). \quad (8)$$

Because $\lim_{z\to z_{s+}} \partial_z G^-(\mathbf{x},\mathbf{x}_s) = 0$, the upgoing Green's function is also discontinuous at the source location.

The Green's functions can be defined either in the physical medium or in a reference medium. We define a specific reference medium, which is reflection-free above boundary $\partial\mathcal{V}_i$ and below boundary $\partial\mathcal{V}_j$. In between these boundaries, the medium properties of the reference medium are identical to the medium properties of the physical medium. We refer to the Green's functions in this specific reference medium with a bar, i.e., $\bar{G}(\mathbf{x},\mathbf{x}_s)$. The Green's functions in the physical medium are indicated without such a bar, i.e., $G(\mathbf{x},\mathbf{x}_s)$. With target-enclosed redatuming, we aim to retrieve the Green's functions in the reference medium from responses in the physical medium, as we have illustrated schematically in Figure 1a and 1b.

Green's function representations at the upper boundary

To derive representations for the Green's function at the upper boundary of the volume $\partial\mathcal{V}_i$, we substitute the wavefield $p_A^{\pm} = G^{\pm}(\mathbf{x},\mathbf{x}_a)$ in the physical medium in state A. Here, $\mathbf{x}_a = (x_a, y_a, z_a)$ is a location at the earth's surface, where $z_a < z_i < z_j$. In state B, we choose the reference medium that we specified in the previous section (which is reflection-free outside the target volume). An impulsive source is positioned at $\mathbf{x}_i$, which is located on the boundary $\partial\mathcal{V}_i$ in the limit from above (such that $\mathbf{x}_i \notin \mathcal{V}$). The resulting pressure field in state B is $p_B^{\pm} = \bar{G}^{\pm}(\mathbf{x},\mathbf{x}_i)$. Because the part of the reference medium above the volume $\mathcal{V}$ is reflection-free, it follows that the downgoing field $\bar{G}^{\pm}(\mathbf{x},\mathbf{x}_i)$ at $\partial\mathcal{V}_i$ can be described by equation 7 with the substitutions $\mathbf{x}_s \to \mathbf{x}_i$ and $G^+ \to \bar{G}^+$. Because the part of the reference medium below $\mathcal{V}$ is also reflection-free, it follows that $\bar{G}^-(\mathbf{x},\mathbf{x}_i)$ and its vertical derivative vanish at $\partial\mathcal{V}_j$. When the relevant wavefields are substituted into equation 4, the following representation of the convolution type can be derived:

$$G^-(\mathbf{x}_i,\mathbf{x}_a) = \int_{\partial\mathcal{V}_i} dxdyG^+(\mathbf{x},\mathbf{x}_a)\frac{2\mathcal{H}_1}{\omega\varrho}\bar{G}^-(\mathbf{x},\mathbf{x}_i) + \int_{\partial\mathcal{V}_j} dxdyG^-(\mathbf{x},\mathbf{x}_a)\frac{2\mathcal{H}_1}{\omega\varrho}\bar{G}^+(\mathbf{x},\mathbf{x}_i). \quad (9)$$

Alternatively, the wavefields can be substituted into equation 5, yielding a representation of the correlation type:

$$G^{+*}(\mathbf{x}_i,\mathbf{x}_a) = \int_{\partial\mathcal{V}_i} dxdyG^{-*}(\mathbf{x},\mathbf{x}_a)\frac{2\mathcal{H}_1}{\omega\varrho}\bar{G}^-(\mathbf{x},\mathbf{x}_i) + \int_{\partial\mathcal{V}_j} dxdyG^{+*}(\mathbf{x},\mathbf{x}_a)\frac{2\mathcal{H}_1}{\omega\varrho}\bar{G}^+(\mathbf{x},\mathbf{x}_i). \quad (10)$$

With equation 9, the upgoing wavefield that leaves volume $\mathcal{V}$ at the upper boundary can be computed by propagating the wavefields that enter the volume forward in time with the Green's functions in the reference medium. With equation 10, we can compute the downgoing wavefield that enters volume $\mathcal{V}$ at the upper boundary by propagating the wavefields that leave the volume backward in time. Alternatively, the representations can be inverted for the Green's functions in the reference medium, given that all Green's functions that enter and leave the volume are known. At this point, we have a system of two equations and four unknowns, which cannot be solved without additional constraints. To condition the inversion, we derive two more representations for the wavefields that leave and enter the volume at the lower boundary.

Green's function representations at the lower boundary

To derive a representation for the wavefields at the lower boundary, we follow the same reasoning as in the previous subsection, except that we place the source in state B at $\mathbf{x}_j$, which is located on the boundary $\partial\mathcal{V}_j$ in the limit from below (such that $\mathbf{x}_j \notin \mathcal{V}$). Because the part of the reference medium below the lower boundary is reflection-free, the upgoing field $\bar{G}^-(\mathbf{x},\mathbf{x}_j)$ at $\partial\mathcal{V}_j$ can be described by equation 8 with the substitutions $\mathbf{x}_s \to \mathbf{x}_j$ and $G^- \to \bar{G}^-$. Because the part of the reference medium above the upper boundary is also reflection-free, it follows that $\bar{G}^+(\mathbf{x},\mathbf{x}_i)$ and its vertical derivative vanish at $\partial\mathcal{V}_i$. Substituting the wavefield quantities into equations 4 and 5 brings us to the representations

$$G^+(\mathbf{x}_j,\mathbf{x}_a) = \int_{\partial\mathcal{V}_i} dxdyG^+(\mathbf{x},\mathbf{x}_a)\frac{2\mathcal{H}_1}{\omega\varrho}\bar{G}^-(\mathbf{x},\mathbf{x}_j) + \int_{\partial\mathcal{V}_j} dxdyG^-(\mathbf{x},\mathbf{x}_a)\frac{2\mathcal{H}_1}{\omega\varrho}\bar{G}^+(\mathbf{x},\mathbf{x}_j) \quad (11)$$

and

$$G^{-*}(\mathbf{x}_j,\mathbf{x}_a) = \int_{\partial\mathcal{V}_i} dxdyG^{-*}(\mathbf{x},\mathbf{x}_a)\frac{2\mathcal{H}_1}{\omega\varrho}\bar{G}^-(\mathbf{x},\mathbf{x}_j) + \int_{\partial\mathcal{V}_j} dxdyG^{+*}(\mathbf{x},\mathbf{x}_a)\frac{2\mathcal{H}_1}{\omega\varrho}\bar{G}^+(\mathbf{x},\mathbf{x}_j). \quad (12)$$

The interpretation of these equations is similar to the interpretation of equations 9 and 10. In equation 11, the field that leaves the volume at the lower boundary is expressed by propagating the fields that enter the volume forward in time, whereas in equation 12, the field that enters the volume at the lower boundary is expressed by propagating the fields that leave the volume backward in time. In the following subsection, we show how equations 9–12 can be jointly inverted for the Green's functions in the reference medium. This is the essence of target-enclosed redatuming.

Inversion of the Green's function representations

Here, we show how equations 9–12 can be inverted to retrieve the Green's functions in the reference medium. Before doing so, we consider the special case where $\partial\mathcal{V}_j$ is below the lowest reflector at $z_j \to +\infty$, such that there are no upgoing waves at this boundary. As a consequence of this choice, the second integral on the right side of equation 9 vanishes, leading to

$$G^-(\mathbf{x}_i,\mathbf{x}_a)=\int_{\partial\mathcal{V}_i}dxdyG^+(\mathbf{x},\mathbf{x}_a)\frac{2\mathcal{H}_1}{\omega\varrho}\hat{G}^-(\mathbf{x},\mathbf{x}_i),\qquad(13)$$

where $\hat{G}^-(\mathbf{x},\mathbf{x}_i)$ denotes the upgoing wavefield in an alternative reference medium, which is reflection-free above $\partial\mathcal{V}_i$, but identical to the physical medium below this boundary. We can discretize the known wavefield $G^-(\mathbf{x}_i,\mathbf{x}_a)$ on the left side as a column vector $\mathbf{g}^-_{ia}$, where the subscripts a and i indicate that the sources and receivers are located on boundaries $\partial\mathcal{V}_a$ and $\partial\mathcal{V}_i$, respectively. In this vector, the data of the source locations $\mathbf{x}_i$ and receiver locations $\mathbf{x}_a$ are concatenated. In a similar way, the unknown Green's function in the reference medium $\hat{G}^-(\mathbf{x},\mathbf{x}_i)$ is discretized as $\hat{\mathbf{g}}^-_{ii}$, where ii indicates that sources and receivers are located on boundary $\partial\mathcal{V}_i$. By using this notation, equation 13 can be written as

$$\mathbf{g}^-_{ia}=\mathbf{A}(G^+_{ia})\boldsymbol{\Upsilon}_R\hat{\mathbf{g}}^-_{ii}.\qquad(14)$$

In Appendix B, we show how to compute matrix $\mathbf{A}(G^+_{ia})$ in the frequency domain. Note that we have introduced matrix $\boldsymbol{\Upsilon}_R$ in equation 14, which is defined as $\boldsymbol{\Upsilon}_R=(1/2)(1+\boldsymbol{\Upsilon}_T)$, where $\boldsymbol{\Upsilon}_T$ is a matrix that interchanges the source and receiver elements in the array. Hence, $\boldsymbol{\Upsilon}_R$ enforces that the retrieved reflection response obeys source-receiver reciprocity, according to $\hat{G}^-(\mathbf{x},\mathbf{x}_i)=\hat{G}^-(\mathbf{x}_i,\mathbf{x})$. Any solution that does not obey this relation lies in the null space of $\boldsymbol{\Upsilon}_R$ and thus cannot be retrieved. Hence, the operator $\boldsymbol{\Upsilon}_R$ can constrain the inversion in case the data are incomplete and in the presence of noise. Further, we note that the square-root operator has been included in the computation of matrix $\mathbf{A}$ (see Appendix B). As a consequence, we retrieve the Green's function of a monopole source when equation 14 is inverted. This deviates from the work of Wapenaar and van der Neut (2010) and others, where the Green's function of a dipole source is retrieved. This choice is made to facilitate local imaging schemes in the target volume that require the Green's functions of monopoles instead of dipoles. Note that the retrieved monopoles can easily be transformed into dipoles by applying the square-root operator (which is computationally more attractive than applying the inverse square-root operator required to transform dipoles into monopoles).

Because each frequency component can be computed and inverted individually, it is computationally attractive to solve equation 14 in the frequency domain. However, because the frequency-domain formulation lacks a constraint on the causality of the solution, it may occur that the retrieved wavefields are (partially) acausal. Equation 14 can also be constructed after transforming the wavefields to the time domain. In this formulation, quantities $\mathbf{g}^-_{ia}$ and $\hat{\mathbf{g}}^-_{ii}$ are to be discretized as column vectors containing all samples in space and time, whereas matrix $\boldsymbol{\Upsilon}_R$ should be applied to time slices, rather than to frequency slices. In Appendix C, we show how matrix $\mathbf{A}(G^+_{ia})$ can be constructed in the time domain. In the time-domain approach, we introduce matrix $\boldsymbol{\Upsilon}_H$, which passes only causal solutions. Because acausal solutions are in the null space of this matrix, causality is enforced. To exploit this advantage, we use the time-domain formulation in all examples shown herein.

After the known quantities in equation 14 have been computed, we can solve the equation, for instance, by least-squares inversion. This strategy has also been referred to as multidimensional deconvolution (Wapenaar and van der Neut, 2010; Ravasi et al., 2015a; van der Neut et al., 2016). In this paper, least-squares inversion is implemented by the LSQR algorithm (Paige and Saunders, 1982). Alternative solvers can also be used, for instance, solvers that promote sparsity of the reference Green's functions in an appropriate transform domain (Tu and Herrmann, 2015). The latter strategy can be beneficial in case of low signal-to-noise levels and incomplete data (Lin and Herrmann, 2016). Alternatively, equation 14 can be rewritten as a Neumann series (van Borselen et al., 1996; van der Neut et al., 2013), providing a numerically stable solution in which adaptive filters can easily be incorporated.

If z_j is not chosen below the lowest reflector, the second integral in equation 9 does not vanish, such that equations 13 and 14 are no longer valid. Now equations 9–12 are to be solved together to obtain the unknown Green's functions in the reference medium, discretized respectively as $\bar{\mathbf{g}}^-_{ii}$, $\bar{\mathbf{g}}^+_{jj}$, $\bar{\mathbf{g}}^-_{ij}$, and $\bar{\mathbf{g}}^+_{ji}$. The number of unknowns can be reduced by recognizing that the transmission response obeys source-receiver reciprocity according to $G^+(\mathbf{x}_j,\mathbf{x}_i)=G^-(\mathbf{x}_i,\mathbf{x}_j)$. This property is enforced by matrix $\boldsymbol{\Upsilon}_T$ that interchanges the entries of sources and receivers, such that $\bar{\mathbf{g}}^-_{ij}=\boldsymbol{\Upsilon}_T\bar{\mathbf{g}}^+_{ji}$. The other Green's functions in equations 9–12 are discretized, using a similar notation as in equation 14. The following inverse problem can now be formulated:

$$\begin{pmatrix}\mathbf{g}^-_{ia}\\ \mathbf{g}^{+*}_{ia}\\ \mathbf{g}^+_{ja}\\ \mathbf{g}^{-*}_{ja}\end{pmatrix}=\begin{pmatrix}\mathbf{A}(G^+_{ia})\boldsymbol{\Upsilon}_R & 0 & \mathbf{A}(G^-_{ja})\\ \mathbf{A}(G^{-*}_{ia})\boldsymbol{\Upsilon}_R & 0 & \mathbf{A}(G^{+*}_{ja})\\ 0 & \mathbf{A}(G^-_{ja})\boldsymbol{\Upsilon}_R & \mathbf{A}(G^+_{ia})\boldsymbol{\Upsilon}_T\\ 0 & \mathbf{A}(G^{+*}_{ja})\boldsymbol{\Upsilon}_R & \mathbf{A}(G^{-*}_{ia})\boldsymbol{\Upsilon}_T\end{pmatrix}\begin{pmatrix}\bar{\mathbf{g}}^-_{ii}\\ \bar{\mathbf{g}}^+_{jj}\\ \bar{\mathbf{g}}^+_{ji}\end{pmatrix}.\qquad(15)$$

In this formulation, matrices $\mathbf{A}(x^{\pm}_{ka})$ can either be computed in the frequency domain (see Appendix B), which is attractive from a computational point of view, or in the time domain (see Appendix C), where the causality constraint can be included. Akin to equation 14, equation 15 can be solved for the unknown Green's functions in the reference medium, using, for instance, LSQR.

TARGET-ENCLOSED REDATUMING WITH FOCUSING FUNCTIONS

As we discussed before, the Green's functions at boundaries $\partial\mathcal{V}_i$ and $\partial\mathcal{V}_j$ can be retrieved by solving a multidimensional Marchenko equation (Wapenaar et al., 2014). The solution of this equation yields, in addition to the surface-to-subsurface Green's functions, the so-called focusing functions at $\partial\mathcal{V}_i$ and $\partial\mathcal{V}_j$. Focusing functions are solutions of the wave-equation subject to specific focusing conditions. In this section, we derive an alternative set of equations for target-oriented redatuming that use focusing functions (rather than the Green's functions) as input.

Focusing functions

We distinguish two focusing functions, which we refer to as $f_1(\mathbf{x},\mathbf{x}_f,\omega)$ and $f_2(\mathbf{x},\mathbf{x}_f,\omega)$, where $\mathbf{x}_f$ is defined as the focal point. Both are functions of the spatial coordinate $\mathbf{x}$ and angular frequency ω. They can be decomposed into downgoing and upgoing constituents, according to $f_1=f_1^+ + f_1^-$ and $f_2=f_2^+ + f_2^-$. The focusing functions are solutions of a source-free wave equation, i.e., equation 1 with $q=0$. The first focusing function is defined in a reference medium, which is identical to the physical medium above the

focal point but reflection-free below this point. The downgoing part of this focusing function f_1^+ focuses at $\mathbf{x}_f$. Unlike the Green's function, which is discontinuous at the source location $\mathbf{x}_s$, the focusing function is continuous at the focal point, where the following focusing condition is specified:

$$\lim_{z\to z_f} \partial_z f_1^+(\mathbf{x},\mathbf{x}_f) = -\frac{j\omega\varrho}{2}\delta(x-x_f)\delta(y-y_f). \tag{16}$$

Here, and in the derivations that follow, we omit the dependence of the focusing functions on angular frequency for notational convenience. Because the half-space below the focal point is reflection-free, the upgoing part of the focusing function f_1^- and its vertical derivative vanish at and below $\mathbf{x}_f$. The second focusing function f_2 is defined in another reference medium, which is identical to the physical medium below the focal point, but it is reflection-free above this location. The upgoing part of this focusing function focuses, which is enforced by the condition

$$\lim_{z\to z_f} \partial_z f_2^-(\mathbf{x},\mathbf{x}_f) = \frac{j\omega\varrho}{2}\delta(x-x_f)\delta(y-y_f). \tag{17}$$

The downgoing part of the second focusing function $f_2^+(\mathbf{x},\mathbf{x}_f)$ and its vertical derivative vanish at and above the focal point because the medium is nonreflective in this region. It can be derived that both focusing functions are related to each other through the symmetry relations $f_1^+(\mathbf{x},\mathbf{x}_f) = f_2^-(\mathbf{x}_f,\mathbf{x})$ and $f_1^-(\mathbf{x},\mathbf{x}_f) = -f_2^{+*}(\mathbf{x}_f,\mathbf{x})$ (Wapenaar et al., 2014).

Focusing function representations at the upper boundary

We start by deriving representations for the focusing function at the upper boundary of the volume $\partial\mathcal{V}_i$. In state A, we substitute the focusing function $p_A^\pm = f_2^\pm(\mathbf{x},\mathbf{x}_a)$, where $\mathbf{x}_a$ is a location at the earth's surface. In state B, we choose the same reference medium as in the previous section, which is identical to the physical medium inside $\mathcal{V}$ but reflection-free outside this volume. This leads to the wavefields $p_B^\pm = \bar{G}^\pm(\mathbf{x},\mathbf{x}_i)$, where the source $\mathbf{x}_i$ is located on the boundary $\partial\mathcal{V}_i$ in the limit from above (such that $\mathbf{x}_i \notin \mathcal{V}$). We find the following representation of the convolution type after substitution of these quantities into equation 4:

$$f_2^-(\mathbf{x}_i,\mathbf{x}_a) = \int_{\partial\mathcal{V}_i} dxdy f_2^+(\mathbf{x},\mathbf{x}_a)\frac{2\mathcal{H}_1}{\omega\varrho}\bar{G}^-(\mathbf{x},\mathbf{x}_i) + \int_{\partial\mathcal{V}_j} dxdy f_2^-(\mathbf{x},\mathbf{x}_a)\frac{2\mathcal{H}_1}{\omega\varrho}\bar{G}^+(\mathbf{x},\mathbf{x}_i). \tag{18}$$

An equivalent representation of the correlation type follows by substituting the wavefields into equation 5:

$$f_2^{+*}(\mathbf{x}_i,\mathbf{x}_a) = \int_{\partial\mathcal{V}_i} dxdy f_2^{-*}(\mathbf{x},\mathbf{x}_a)\frac{2\mathcal{H}_1}{\omega\varrho}\bar{G}^-(\mathbf{x},\mathbf{x}_i) + \int_{\partial\mathcal{V}_j} dxdy f_2^{+*}(\mathbf{x},\mathbf{x}_a)\frac{2\mathcal{H}_1}{\omega\varrho}\bar{G}^+(\mathbf{x},\mathbf{x}_i). \tag{19}$$

Note that these representations have the same structure as equations 9 and 10. This makes intuitive sense because the Green's functions and the focusing functions are solutions of the wave equation, which can be extrapolated forward and backward with the Green's functions in the reference medium.

Focusing function representations at the lower boundary

Equivalent representations can be derived for the focusing function at the lower boundary. To do so, we repeat the derivation of the previous subsection with the source in state B at $\mathbf{x}_j$ on the boundary $\partial\mathcal{V}_j$ in the limit from below (such that $\mathbf{x}_j \notin \mathcal{V}$). This leads to a representation of the convolution type

$$f_2^+(\mathbf{x}_j,\mathbf{x}_a) = \int_{\partial\mathcal{V}_i} dxdy f_2^+(\mathbf{x},\mathbf{x}_a)\frac{2\mathcal{H}_1}{\omega\varrho}\bar{G}^-(\mathbf{x},\mathbf{x}_j) + \int_{\partial\mathcal{V}_j} dxdy f_2^-(\mathbf{x},\mathbf{x}_a)\frac{2\mathcal{H}_1}{\omega\varrho}\bar{G}^+(\mathbf{x},\mathbf{x}_j), \tag{20}$$

and a representation of the correlation type

$$f_2^{-*}(\mathbf{x}_j,\mathbf{x}_a) = \int_{\partial\mathcal{V}_i} dxdy f_2^{-*}(\mathbf{x},\mathbf{x}_a)\frac{2\mathcal{H}_1}{\omega\varrho}\bar{G}^-(\mathbf{x},\mathbf{x}_j) + \int_{\partial\mathcal{V}_j} dxdy f_2^{+*}(\mathbf{x},\mathbf{x}_a)\frac{2\mathcal{H}_1}{\omega\varrho}\bar{G}^+(\mathbf{x},\mathbf{x}_j). \tag{21}$$

Once again, the analogy with equations 11 and 12 is clear, making target-enclosed redatuming with focusing functions in principle a feasible objective, in the sense that we obtain a system of four equations with four unknowns.

Inversion of the focusing function representations

Before we discuss the joint inversion of equations 18–21, we consider a special case where the upper boundary is placed at the earth's surface; i.e., $z_i = z_a$. In this case, the first integral on the right side of equation 20 vanishes, leaving us with

$$f_2^+(\mathbf{x}_j,\mathbf{x}_a) = \int_{\partial\mathcal{V}_j} dxdy f_2^-(\mathbf{x},\mathbf{x}_a)\frac{2\mathcal{H}_1}{\omega\varrho}\tilde{G}^+(\mathbf{x},\mathbf{x}_j). \tag{22}$$

Here, we have introduced $\tilde{G}^+$ as the Green's function of an alternative reference medium, which is identical to the physical medium above the lower boundary $\partial\mathcal{V}_j$ but reflection-free below this boundary. To retrieve this Green's function, we can discretize equation 22 as

$$\mathbf{f}_{ja}^+ = \mathbf{A}(f_{ja}^-)\boldsymbol{\Upsilon}_R\tilde{\mathbf{g}}_{jj}^+, \tag{23}$$

where we used the same function $\mathbf{A}(x_{ka}^\pm)$ as before, which can be computed in the frequency domain (see Appendix B) or in the time domain (see Appendix C). This equation can be solved for $\tilde{\mathbf{g}}_{jj}^+$, for instance by least-squares inversion. This approach leads to a Green's function in a reference medium, which is reflection-free below the lower boundary. These Green's functions can be used to image targets

from below (Ravasi et al., 2016). If we choose the upper boundary below the earth's surface, equations 22 and 23 are no longer valid. However, we can still retrieve target-enclosed extended images by solving the system of equations 18–21. This system can be discretized as

$$\begin{pmatrix} \mathbf{f}^{-}_{ia} \\ \mathbf{f}^{+*}_{ia} \\ \mathbf{f}^{+}_{ja} \\ \mathbf{f}^{-*}_{ja} \end{pmatrix} = \begin{pmatrix} \mathbf{A}(f^{+}_{ia})\boldsymbol{\Upsilon}_R & \mathbf{0} & \mathbf{A}(f^{-}_{ja}) \\ \mathbf{A}(f^{-*}_{ia})\boldsymbol{\Upsilon}_R & \mathbf{0} & \mathbf{A}(f^{+*}_{ja}) \\ \mathbf{0} & \mathbf{A}(f^{-}_{ja})\boldsymbol{\Upsilon}_R & \mathbf{A}(f^{+}_{ia})\boldsymbol{\Upsilon}_T \\ \mathbf{0} & \mathbf{A}(f^{+*}_{ja})\boldsymbol{\Upsilon}_R & \mathbf{A}(f^{-*}_{ia})\boldsymbol{\Upsilon}_T \end{pmatrix} \begin{pmatrix} \bar{\mathbf{g}}^{-}_{ii} \\ \bar{\mathbf{g}}^{+}_{jj} \\ \bar{\mathbf{g}}^{+}_{ji} \end{pmatrix}. \tag{24}$$

Equation 24 is an alternative formulation that can be used to invert for the Green's functions in the reference medium. Although this formulation seems different than the formulation based on the Green's functions (i.e., equation 15), we show later in this paper that both formulations are intrinsically related, given that the Green's functions and focusing functions are retrieved by solving the multidimensional Marchenko equation.

NUMERICAL EXAMPLES

In this section, we illustrate the theory with an example in a 2D synthetic medium. We select an acquisition boundary $\mathcal{S}_a$ at the top of the medium, and a target zone $\mathcal{V}$ with two enclosing boundaries $\partial\mathcal{V}_i$ and $\partial\mathcal{V}_j$. We retrieve the Green's functions and focusing functions at the enclosing boundaries from reflection data at the acquisition boundary by solving a multidimensional Marchenko equation. These functions are used for target-enclosed redatuming by solving the inverse problems in equations 15 and 24. Finally, we show how the retrieved target-enclosed extended images can be used to image the target volume from above and from below, as well as for two-sided imaging.

The model

In Figure 2a, we show the 2D synthetic model, which we refer to as the physical medium. We place 301 colocated sources and receivers every 10 m on a fixed grid at the acquisition boundary $\mathcal{S}_a$, indicated by the black line at $z = 0$ m. Shot records are obtained by finite-difference modeling with a flat-spectrum source wavelet and a time sampling of 4ms. Two boundaries $\partial\mathcal{V}_i$ and $\partial\mathcal{V}_j$ are selected at $z = 750$ and 1500 m, respectively, enclosing the target zone. At each boundary, we define an array that is sampled by 301 focal points with 10 m spacing. Like the acquisition array at $\mathcal{S}_a$, these arrays have a finite length of 3000 m. For simplicity, the density is constant throughout the medium ($\varrho = 1000$ kg m^{-3}). We emphasize that constant density is not a fundamental assumption for the application of the methodology. The multidimensional Marchenko equation can be solved in media with arbitrary velocity and density contrasts (Broggini et al., 2014; Singh and Snieder, 2017), which is equally true for redatuming by inversion, given that the wavefields at the redatuming boundaries are known (Wapenaar and van der Neut, 2010). It is required, however, that the medium properties $c(\mathbf{x})$ and $\varrho(\mathbf{x})$ vary only smoothly in the lateral direction at and around the redatuming boundaries. It is well-understood that discontinuity of the medium properties at these boundaries can complicate the numerical computation of the square-root operators (Grimbergen et al., 1998). The effects of such discontinuities on solving the multidimensional Marchenko equation (Meles et al., 2016) and on redatuming by inversion (Ravasi et al., 2015a) have been described in the existing literature, too. To avoid these complications, we have designed the medium properties to be constant at both redatuming boundaries. The consequences of a complex overburden for (1) solving the multidimensional Marchenko equation (van der Neut et al., 2015; Vasconcelos et al., 2015) and (2) redatuming by inversion (Wapenaar and van der Neut, 2010; Ravasi et al., 2015a) have also been studied already. Because these consequences are not directly relevant for our current objectives, we have designed the part of the medium above $\partial\mathcal{V}_i$ to be relatively simple. The target zone (which is selected from the Sigsbee model of Paffenholz et al., 2002) and the part of the medium below $\partial\mathcal{V}_j$ are more complex.

To retrieve the Green's functions and focusing functions from the multidimensional Marchenko equation, we require knowledge of the direct wavefield as it propagates from the acquisition array at $\mathcal{S}_a$ to the redatuming arrays at $\partial\mathcal{V}_i$ and $\partial\mathcal{V}_j$. For this purpose, we typically use a macro model of the propagation velocity (Broggini et al., 2014). As a starting point, we compute wavefields by finite-difference modeling in the exact medium and we separate the direct components with a time gate. These direct wavefields are used to solve the multidimensional Marchenko equation (Wapenaar et al., 2014). We refer to the wavefields retrieved in this way as kinematically correct Green's functions and focusing functions. To quantify the effects of velocity mismatch in the target zone, we also compute the approximate Green's functions and the focusing functions. Unlike the kinematically correct functions, these functions have been retrieved using direct wavefields (which are also isolated with a time gate) in a smooth model, as shown in Figure 2b. Because it is well-understood that velocity errors above $\partial\mathcal{V}_i$ result in blurring of the redatumed gathers, which is already described in the existing literature (Broggini et al., 2014), we have chosen the part of the macro model at greater than $\partial\mathcal{V}_i$ to be identical to the physical medium. The medium properties of the target zone have been smoothed. The consequence of using approximate Green's functions and focusing func-

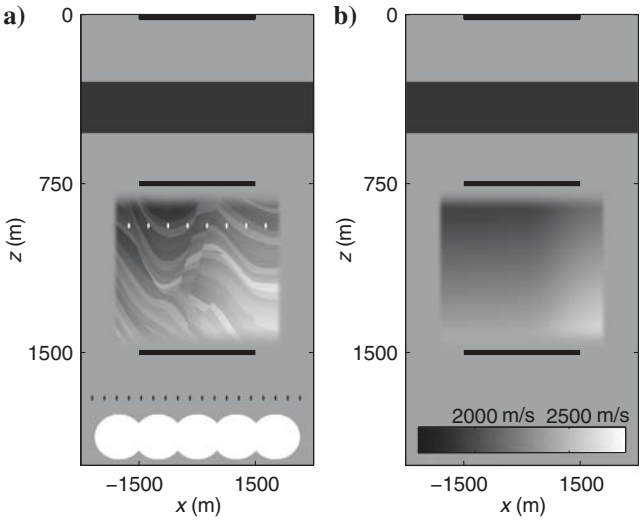

Figure 2. (a) Propagation velocity in the physical medium (the color bar is shown in [b]). (b) Macro velocity model with color bar. The black lines at $z = 0$, 750, and 1500 m indicate arrays at boundaries $\mathcal{S}_a$, $\partial\mathcal{V}_i$, and $\partial\mathcal{V}_j$, respectively. The target zone is defined as the part of the medium where $z \in [750, 1500$ m].

tions instead of their kinematically correct counterparts is one of the key issues that will be discussed later in this paper.

One of the 301 shot records that have been computed at $z = 0$ is displayed in Figure 3a. We can recognize the two reflectors above $\partial\mathcal{V}_i$ at $t_{zo} < 0.7$ s, the target zone at $0.7 \text{ s} < t_{zo} < 1.4$ s and the part of the medium below $\partial\mathcal{V}_j$ thereafter. Here, we have defined t_{zo} as the two-way traveltime at zero offset. In Figure 3b, we show the direct wavefield at $\partial\mathcal{V}_j$, computed in the exact model and isolated by a time gate. An analogous direct wavefield is computed at the upper boundary $\partial\mathcal{V}_i$. These wavefields are used to solve the multidimensional Marchenko equation (Wapenaar et al., 2014), leading to the required kinematically correct Green's functions and focusing functions at $\partial\mathcal{V}_i$ and $\partial\mathcal{V}_j$. Later in the paper, we will also use the approximate Green's functions and focusing functions (computed from direct wavefields in the macro model).

Target-enclosed redatuming

The multidimensional Marchenko equation is solved to retrieve the kinematically correct Green's functions and focusing functions at the boundaries $\partial\mathcal{V}_i$ and $\partial\mathcal{V}_j$. For this purpose, we have used the reflection data and the direct wavefields from the acquisition boundary $\mathcal{S}_a$ to the redatuming boundaries, which we have computed in the physical medium. First, we analyze the retrieved transmission responses $\bar{G}^{+}(\mathbf{x}, \mathbf{x}_i)$ with $\mathbf{x} \in \partial\mathcal{V}_j$. In Figure 3c, we show a shot record with a source at the upper boundary $\partial\mathcal{V}_i$ and receivers at the lower boundary $\partial\mathcal{V}_j$. This record is computed in a reference medium, which is homogeneous outside the target zone. This is the response that we would ideally like to retrieve. The response has been amplified with a factor of 20 to enhance diffracted arrivals. In Figure 3d, we show the result that was retrieved by target-enclosed redatuming of the Green's functions (i.e., equation 15), which has also been enhanced by the same factor of 20. We observe that the direct wavefield has been retrieved accurately, whereas the diffracted arrivals are underestimated. This observation can be attributed to the fact that the forward-scattered wavefield has not been included in the direct wavefield that we used to solve the multidimensional Marchenko equation (van der Neut et al., 2015). This can be improved by using a more complicated direct wavefield, as shown by Vasconcelos et al. (2015).

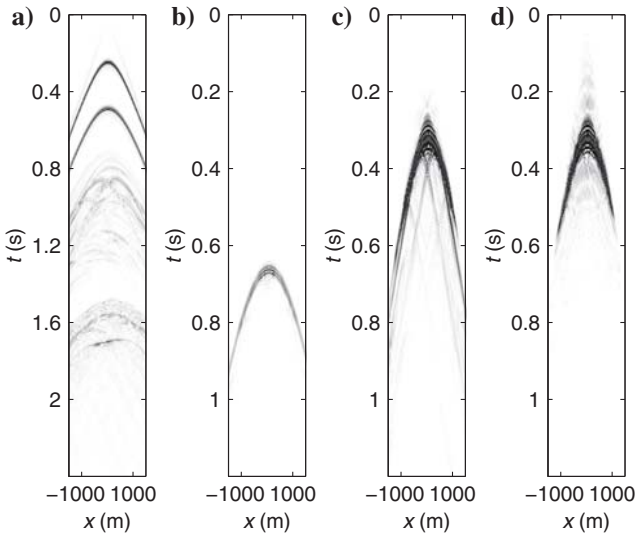

Figure 3. (a) Reflection response with a source at $x = 0$ at the acquisition boundary $\mathcal{S}_a$ and receivers at the same boundary. (b) Direct wavefield with a source at $x = 0$ at $\mathcal{S}_a$ and receivers at $\partial\mathcal{V}_j$, computed by time gating the transmitted wavefield in the physical medium. (c) Transmission response from above with a source at $x = 0$ at $\partial\mathcal{V}_i$ and receivers at $\partial\mathcal{V}_j$, computed in the reference medium. (d) Similar transmission response, obtained by target-enclosed redatuming of the Green's functions (i.e., inversion of equation 15). All figures have been normalized with respect to their maximum value. Panels (c and d) have been enhanced by a factor 20 and are clipped at 5% of the maximum value to emphasize weak arrivals.

Next, we analyze the retrieved reflection responses from above. In Figure 4a, we show a shot record with a source at $\mathbf{x}_i$ and receivers at $\mathbf{x} \in \partial\mathcal{V}_i$, computed directly in the reference medium (i.e., $\bar{G}^{-}(\mathbf{x}, \mathbf{x}_i)$). In Figure 4b, we show the response $\hat{G}^{-}(\mathbf{x}, \mathbf{x}_i)$, which has been retrieved by single-sided redatuming (i.e., inversion of equation 14), where we ran 25 iterations of LSQR. This methodology has been referred to as multidimensional deconvolution, which has been discussed extensively in the literature (Wapenaar and van der Neut, 2010; Ravasi et al., 2015a). As discussed earlier, this methodology yields the response of an alternative reference medium, which is homogeneous above $\partial\mathcal{V}_i$ but identical to the physical medium below this boundary (and below $\partial\mathcal{V}_j$). Hence, the reflectors below the lower boundary $\partial\mathcal{V}_j$ are also retrieved. These reflectors are indeed clearly visible at $t_{zo} > 0.8$ s in Figure 4b. Alternatively, we can retrieve $\bar{G}^{-}(\mathbf{x}, \mathbf{x}_i)$ by target-enclosed redatuming of the Green's functions or focusing functions (i.e., inversion of equation 15 or 24). We show the results after 25 iterations of LSQR in Figure 4c and 4d. Note that the reflectors from below the lower boundary at $t_{zo} > 0.8$ s have indeed been suppressed by both schemes. More specifically: These reflectors can still be observed after 25 iterations in Figure 4c, whereas they are absent in Figure 4d.

We can intuitively understand these observations from the nature of both inverse problems. By applying the adjoint (indicated by superscript †) of the forward operator to the left side of equation 15,

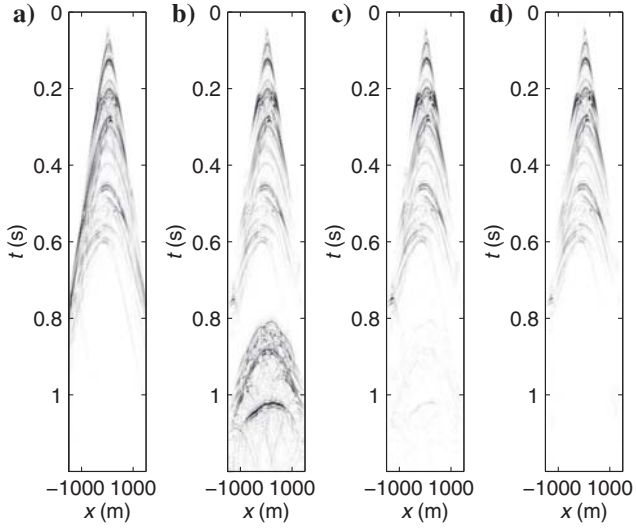

Figure 4. (a) Reflection response from above with a source at $x = 0$ at $\partial\mathcal{V}_i$ and receivers at the same level, computed in the reference medium. (b) Similar reflection response, retrieved by single-sided redatuming of the Green's functions (i.e., inversion of equation 14). Similar reflection responses, retrieved by target-enclosed redatuming of (c) the Green's functions (i.e., inversion of equation 15) and (d) focusing functions (i.e., inversion of equation 24). All figure parts have been normalized with respect to their maximum value.

we find as an initial estimate of the desired Green's function: $\bar{\mathbf{g}}_{ii}^{-} \approx \boldsymbol{\Upsilon}_R^{\dagger}\mathbf{A}^{\dagger}(G_{ia}^{+})\mathbf{g}_{ia}^{-} + \boldsymbol{\Upsilon}_R^{\dagger}\mathbf{A}^{\dagger}(G_{ia}^{-*})\mathbf{g}_{ia}^{+*}$. In this estimate, the reflectors below the target are retrieved mainly by crosscorrelation of primary upgoing reflections $\mathbf{g}_{ia}^{-}$ with the downgoing direct wavefield by $\mathbf{A}^{\dagger}(G_{ia}^{+})$. These reflectors should be removed during subsequent iterations. Hence, the residual of these reflectors in Figure 4d depends on the number of iterations and can be further reduced by increasing this number. The situation is different for inverse problem 24. Because this problem depends on focusing functions only, which are independent on the part of the medium below $\partial\mathcal{V}_j$, these reflectors will never appear in any iteration of the scheme.

Target-enclosed redatuming can also be used to retrieve the reflection response from below the target zone. As a reference, we place a source at $\mathbf{x}_j$ below the target in the reference medium and we compute the response $\bar{G}^{+}(\mathbf{x}, \mathbf{x}_j)$ at the lower boundary (see Figure 5a). In Figure 5b, we show an equivalent result $G^{+}(\mathbf{x}, \mathbf{x}_j)$, which is retrieved by solving inverse problem 23 by 25 iterations of LSQR. This methodology has been used before to image target structures from below (Ravasi et al., 2016). As discussed earlier, this methodology yields a response in an alternative reference medium, which is homogeneous below $\partial\mathcal{V}_j$, but identical to the physical medium above this level (and above $\partial\mathcal{V}_i$). Hence, the strong reflectors in the shallow part of the medium ($z < 1500$ m), which cannot be observed in Figure 5a, are clearly visible in Figure 5b (at $t_{zo} > 0.8$ s). Target-enclosed redatuming allows us to remove these reflectors from the gathers, as demonstrated in Figure 5c and 5d. To obtain these results, we ran 25 iterations of LSQR on inverse problems 15 and 24. We observe that the reflectors at $t_{zo} > 0.8$ s are completely absent for the scheme that is based on the Green's functions (Figure 5c). For the scheme that is based on focusing functions, however, these reflectors are still weakly visible (Figure 5d).

To understand these observations intuitively, we consider the initial estimates that can be obtained by applying the adjoints of the forward operators to the left sides of equations 15 and 24. For the scheme that is based on focusing functions (equation 24), we find for the initial estimate: $\bar{\mathbf{g}}_{jj}^{+} \approx \boldsymbol{\Upsilon}_R^{\dagger}\mathbf{A}^{\dagger}(f_{ja}^{-})\mathbf{f}_{ja}^{+} + \boldsymbol{\Upsilon}_R^{\dagger}\mathbf{A}^{\dagger}(f_{ja}^{+*})\mathbf{f}_{ja}^{-*}$. In this initial estimate, the reflectors at $t_{zo} > 0.8$ s are mainly retrieved by the crosscorrelation of primary reflections in the downgoing focusing function $\mathbf{f}_{ja}^{+}$ with the direct wave in the upgoing focusing function by $\mathbf{A}^{\dagger}(f_{ja}^{-})$. These reflectors should be removed during subsequent iterations. Consequently, Figure 5d can be further improved by increasing the number of iterations. For the scheme that is based on the Green's functions (equation 15), we find $\bar{\mathbf{g}}_{jj}^{+} \approx \boldsymbol{\Upsilon}_R^{\dagger}\mathbf{A}^{\dagger}(G_{ja}^{-})\mathbf{g}_{ja}^{+} + \boldsymbol{\Upsilon}_R^{\dagger}\mathbf{A}^{\dagger}(G_{ja}^{+*})\mathbf{g}_{ja}^{-*}$. Although the reflectors at $t_{zo} > 0.8$ s appear in this initial estimate (by crosscorrelations of internal multiples in the downgoing Green's function $\mathbf{g}_{ja}^{+}$ with primary reflections in the upgoing Green's function by $\mathbf{A}^{\dagger}(G_{ja}^{-})$), these spurious arrivals are relatively weak and they are quickly suppressed in higher order iterations.

Target-enclosed imaging

The reflection responses that have been retrieved can be used to image the target zone from above or from below. This can be achieved by propagating the redatumed wavefields backward into the target zone with help of the macro model in Figure 2b, and crosscorrelating them with their associated source fields, which are propagated forward in the same model. If we evaluate the crosscorrelation at zero time at each image point in the model, an image can be created. We refer to the result as a linear image because only primary reflections are considered (Claerbout, 1971; Berkhout, 1980). In Figure 6a, we show a linear image of the target zone, where we used the redatumed reflection response from above, as retrieved from the kinematically correct focusing functions. Because all interactions with the part of the medium below the target zone arrive after the deepest reflection in the image, this result is almost similar to a conventional Marchenko image, as defined by Wapenaar et al. (2014). Because various authors have already compared Marchenko images (such as in Figure 6a) with the results from standard imaging methods (Broggini et al., 2014; Wapenaar et al., 2014), we consider such a comparison superfluous herein. Instead, we consider Figure 6a as a reference image to be compared with the results from alternative imaging strategies. In Figure 6b, we show a linear image, where we used the redatumed reflection response from below (which we also retrieved from the kinematically correct focusing functions). This image has been multiplied by -1, such that it has the same polarity as the image from above. Because all interactions with the part of the medium above the target zone arrive after the shallowest reflection in the image, this result is almost similar to a Marchenko image from below, as defined by Ravasi et al. (2016). Note that the images from above and below are slightly different from each other. For instance, some of the point diffractors at $z = 940$ m have been shifted downward in Figure 6b in relation to Figure 6a, where they are more accurately positioned. We also note that some reflectors are mispositioned in the image from below and have a different signature compared with the image from above. One example is highlighted by a black circle in the figure parts. To understand these differences, we should realize that the velocity model that is used to solve the Marchenko equation (the physical medium) is different from the velocity model that is used for imaging (the macro model). The situation is different if we use the approximate focusing functions, rather than the kinematically correct focusing functions, for redatuming. For this scenario, the linear images from above and below are highly similar

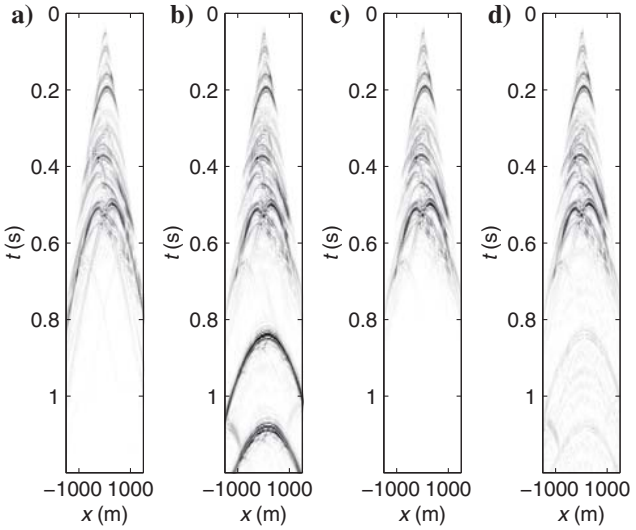

Figure 5. (a) Reflection response from below with a source at $x = 0$ on $\partial\mathcal{V}_j$ and receivers on the same level, computed in the reference medium. A similar reflection response, retrieved by single-sided redatuming of focusing functions (i.e., inversion of equation 23). Similar reflection responses, retrieved by target-enclosed redatuming of the (c) Green's functions (i.e., inversion of equation 15) and (d) focusing functions (i.e., inversion of equation 24). All figure parts have been normalized with respect to their maximum value.

(see Figure 6c and 6d). The only slight difference that can be observed is that in the image from below we have lost resolution at the sides of the model compared with the image from above (note, for instance, the leftmost and rightmost point diffractors at $z = 940$ m).

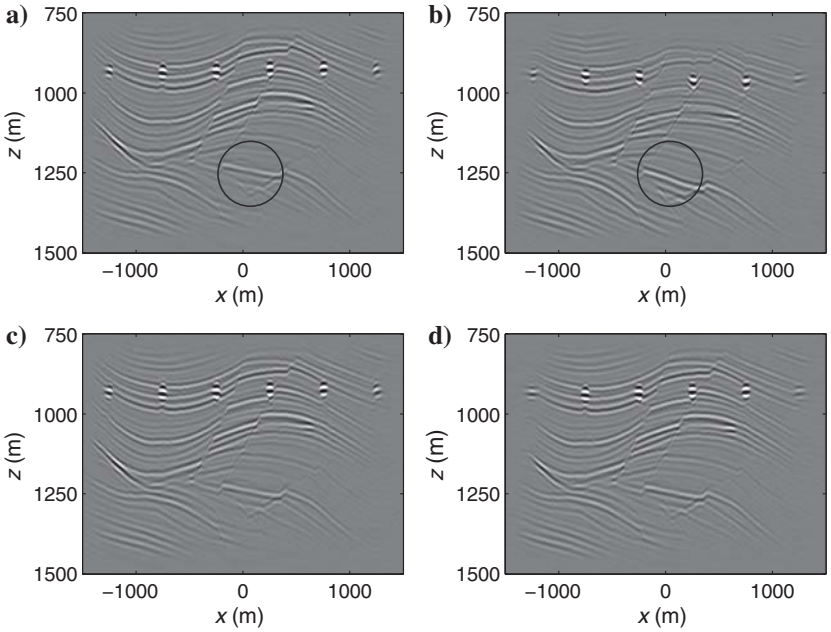

Figure 6. Linear images of the target from (a) above and (b) below after redatuming with kinematically correct focusing functions. The black circles highlight a reflector that is discussed in the main text. Linear image of the target from (c) above and (d) below after redatuming with approximate focusing functions. Here, linear imaging is defined as imaging of primary reflections in the macro model. The images from below have been multiplied with −1 such that all images have the same polarity.

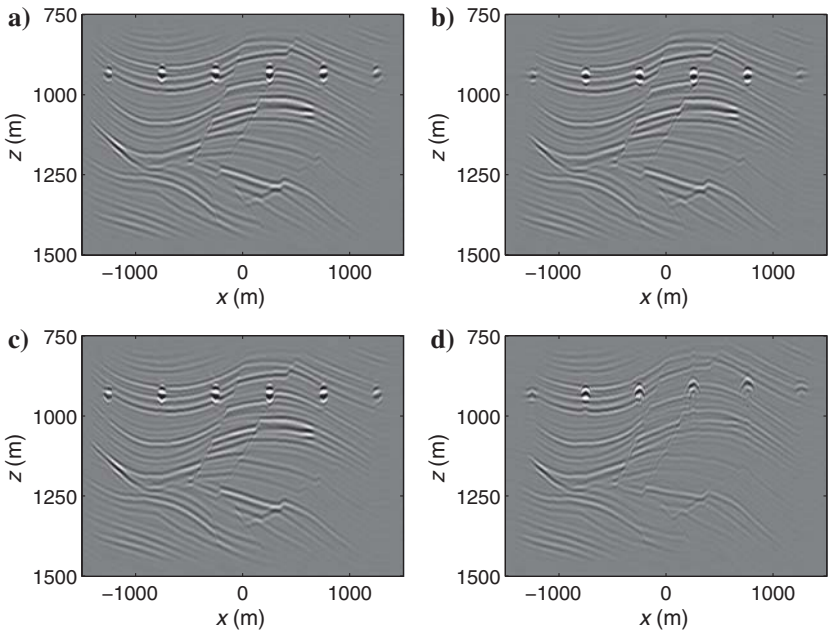

Figure 7. Nonlinear images of the target from (a) above and (b) below after redatuming with kinematically correct focusing functions. Nonlinear images of the target from (c) above and (d) below after redatuming with approximate focusing functions. Here, nonlinear imaging is defined as imaging in the physical medium. The images from below are multiplied with −1, such that all images have the same polarity.

With detailed subsurface models becoming more easily available in geophysics, the use of these models in seismic imaging is starting to be explored (Valenciano and Chemingui, 2015). By propagating wavefields backward in a detailed subsurface model, rather than in a smooth macro model, and crosscorrelating them with their associated source fields in the detailed model, we can image the primary reflections and internal multiples to improve seismic resolution (Youn and Zhou, 2001; Malcolm et al., 2009; Vasconcelos et al., 2010). Because internal multiples are used in this image, this strategy has also been referred to as nonlinear imaging (Fleury and Vasconcelos, 2012; Ravasi et al., 2014). Figure 7 is equivalent to Figure 6, apart from the fact that imaging has been conducted in the physical medium. Note that Figure 7a and 7b is highly similar because the same model is used for redatuming and for imaging, whereas Figure 7c and 7d is different because a different model is used for redatuming than for imaging. Steep dips such as faults have been imaged more accurately in Figure 7a compared with Figure 6a, confirming the value of internal multiples to improve seismic resolution as claimed in the literature on nonlinear imaging (Ravasi et al., 2015b).

Because we have retrieved not only the reflection responses from above and below, but also the transmission response of the target, we might as well propagate the wavefields back into the target zone from the upper and the lower boundaries. By crosscorrelating these back-propagated wavefields with forward-propagated source fields from the same two boundaries, we can evaluate a two-sided nonlinear imaging condition (Ravasi et al., 2014). Unlike in the previous images, the reflection responses and the transmission responses contribute to this result. The contribution from the transmission responses is shown in Figure 8a. To obtain the two-sided nonlinear image, this image should be added to the nonlinear images from above (i.e., Figure 7a) and from below (i.e., Figure 7b with reversed polarity), yielding the image in Figure 8b. Note the superior image quality that can be achieved by this procedure, provided that an accurate subsurface model is available. We conclude this section with Figure 8c and 8d, which are equivalent to Figure 8a and 8b, apart that approximate rather than kinematically correct focusing functions have been used for target-enclosed redatuming. We observe that these images are slightly defocused, which can once again be understood from the fact that a different velocity model has been used for redatuming than for imaging.

DISCUSSION

In this section, we address a few questions that have arisen from the observations in the previous section. First, we compare the target-enclosed redatuming scheme that is based on Green's func-

tions to the scheme that is based on focusing functions. Then, we discuss whether images that are generated "from below" carry additional information compared with the images that are generated "from above." Finally, we discuss the value of target-enclosed redatuming for linear versus nonlinear imaging.

Green's functions or focusing functions?

We have derived a target-enclosed redatuming scheme that is based on Green's functions and an alternative scheme that is based on focusing functions. The scheme that is based on Green's function seems most straightforward in cases in which physical measurements are obtained at the redatuming levels, for instance, by deploying seismic receivers in boreholes (Byun et al., 2010). But which scheme is to be preferred if the Green's functions and focusing functions are retrieved by solving the multidimensional Marchenko equation? In that case, the wavefields are intrinsically related by the following fundamental representation of the convolution type (Wapenaar et al., 2014):

$$G^{-}(\mathbf{x}_i,\mathbf{x}_a)=f_2^{+*}(\mathbf{x}_i,\mathbf{x}_a)+\int_{\mathcal{S}_a} dx'dy'R(\mathbf{x}',\mathbf{x}_a)f_2^{-}(\mathbf{x}_i,\mathbf{x}'), \tag{25}$$

and by an equivalent representation of the correlation type:

$$G^{+}(\mathbf{x}_i,\mathbf{x}_a)=f_2^{-*}(\mathbf{x}_i,\mathbf{x}_a)+\int_{\mathcal{S}_a} dx'dy'R(\mathbf{x}',\mathbf{x}_a)f_2^{+}(\mathbf{x}_i,\mathbf{x}'), \tag{26}$$

where $\mathcal{S}_a$ is the acquisition boundary at $z=0$ and $\mathbf{x}_a\in\mathcal{S}_a$. In this representation, $R(\mathbf{x}',\mathbf{x}_a)=[2\mathcal{H}_1G^{-}(\mathbf{x}',\mathbf{x}_a)]/\omega\rho$ should be interpreted as the reflection response at $\mathcal{S}_a$. When we solve the multidimensional Marchenko equation, we retrieve the upgoing and downgoing focusing function $f_2^{\pm}$ from this reflection response and an estimate of the direct wavefield as it propagates in the macro model. In a secondary step, the upgoing and downgoing Green's functions are computed by evaluation of equations 25 and 26 (Wapenaar et al., 2014). Hence, these equations can be used to express our estimates of the Green's functions directly in terms of our estimates of the focusing functions. If we substitute equations 25 and 26 into Green's function representation 9, it follows that

$$\begin{aligned}
&\int_{\mathcal{S}_a} dx'dy'R(\mathbf{x}',\mathbf{x}_a)f_2^{-}(\mathbf{x}_i,\mathbf{x}')+f_2^{+*}(\mathbf{x}_i,\mathbf{x}_a)\\
&=\int_{\partial\mathcal{V}_i} dxdy\Bigg(f_2^{-*}(\mathbf{x}_i,\mathbf{x}_a)\\
&+\int_{\mathcal{S}_a} dx'dy'R(\mathbf{x}',\mathbf{x}_a)f_2^{+}(\mathbf{x}_i,\mathbf{x}')\Bigg)\frac{2\mathcal{H}_1}{\omega\varrho}\bar{G}^{-}(\mathbf{x}_i,\mathbf{x}_i)\\
&+\int_{\partial\mathcal{V}_j} dxdy\Bigg(f_2^{+*}(\mathbf{x}_j,\mathbf{x}_a)\\
&+\int_{\mathcal{S}_a} dx'dy'R(\mathbf{x}',\mathbf{x}_a)f_2^{-}(\mathbf{x}_j,\mathbf{x}')\Bigg)\frac{2\mathcal{H}_1}{\omega\varrho}\bar{G}^{+}(\mathbf{x}_j,\mathbf{x}_i).
\end{aligned} \tag{27}$$

The exact same result can be obtained from the focusing function representations by convolving equation 18 (with $\mathbf{x}_a$ replaced by $\mathbf{x}'$) with $R(\mathbf{x}',\mathbf{x}_a)$, integrating x' and y' over $\mathcal{S}_a$ and adding equation 19. Hence, equation 9 can be interpreted as a linear superposition of equations 18 and 19 (given that all wavefields are retrieved by the multidimensional Marchenko equation). With an equivalent derivation, we can show that equation 10 is also a linear superposition of equations 18 and 19, whereas equations 11 and 12 are linear superpositions of equations 20 and 21. Consequently, all rows of the matrix in equation 15 can be constructed by linear superpositions of the rows of the matrix in equation 24. Hence, it can be concluded that no additional information is used in the scheme with the Green's functions, compared with the information that is embedded in the focusing functions. It is observed, though, that with 25 iterations of LSQR, the two schemes lead to different results (compare for instance Figure 4c with 4d or 5c with 5d). It can be reasoned that reorganizing the rows as in equation 15 (compared with the rows in equation 24) acts as a preconditioner to the inverse problem, which explains our observations. Because the focusing functions are independent on the part of the medium below $\partial\mathcal{V}_j$, we conclude that both redatuming schemes are independent on this part of the medium. We emphasize that this is not the case when physical recordings are being used, such that the complexities below the lower array can enrich the wavenumber content of the upgoing wavefield, with a potential to improve the seismic resolution (Schuster, 2009). Because equation 15 can be derived from equation 24 by applying a preconditioning matrix (although the inverse of this matrix may not exist), we consider equation 24 to be the most natural starting point for inversion.

Imaging from above or below?

At this point, we have shown that the redatumed data depend only on the focusing functions, which are independent on the medium properties below the target volume. When we study the mechanism

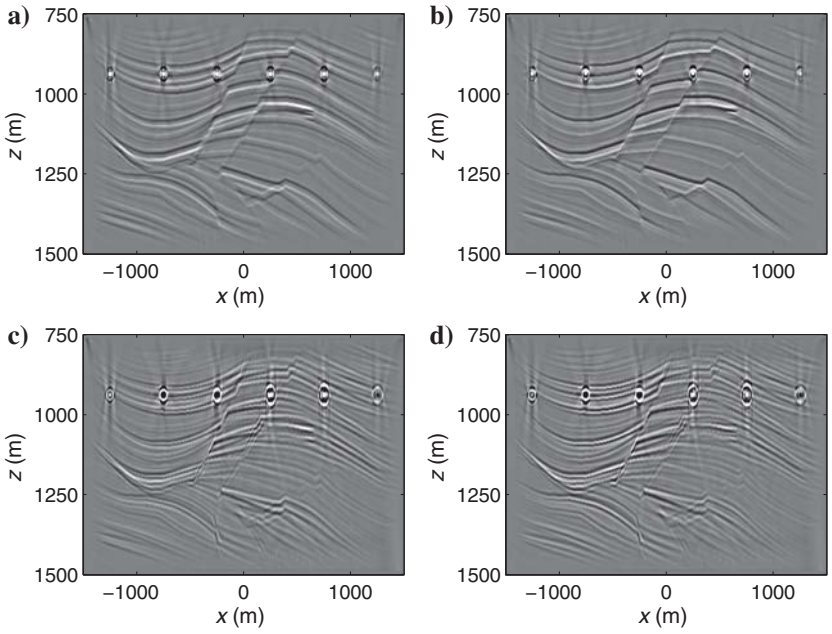

Figure 8. (a) Nonlinear transmission image and (b) two-sided nonlinear image after redatuming with kinematically correct focusing functions. (c) Nonlinear transmission image and (d) two-sided nonlinear image after redatuming with approximate focusing functions. Here, nonlinear imaging is defined as imaging in the physical medium.

by which the individual events of the focusing functions are being constructed, it is observed that we can only retrieve events within the spatial bandwidth that is illuminated by the direct wavefield (van der Neut et al., 2015). Hence, the retrieved reflection response from below can never illuminate a reflector in the target zone under a specific angle if this reflector is not illuminated under the same angle from above. Consequently, the linear image from below does not contain additional information compared with the image from above. This statement is backed by the images in Figure 6c and 6d or 7a and 7b, where illumination from below does not seem to bring any sign of improvement (despite the fact that the point diffractors in the deeper part of the medium in Figure 2a enhance the wavenumber content of the reflected wavefield). This may be improved, though, by using a more developed direct wavefield, which includes forward-scattered arrivals, to solve the multidimensional Marchenko equation (Vasconcelos et al., 2015). Such modification is beyond the scope of this paper.

As mentioned before, we observe a slight deterioration in the images from below, compared with the images from above. To understand these observations intuitively, we should realize that redatuming acts as a spatial filter to the data (Wapenaar and van der Neut, 2010). Because this filter is narrower for the deep array at $\partial\mathcal{V}_j$ than for the shallow array at $\partial\mathcal{V}_i$, the resolution that can be achieved from the shallow array will always be equal to or superior to the resolution that can be achieved from the deep array. Once more, we emphasize that the situation is different when physical receivers are deployed at the lower boundary. In this case, the reflected wavefield from below the target has the potential to enrich the illumination in the image from below, as discussed before. Moreover, the kinematic variations in Figure 6a and 6b confirm previous studies with physical receivers in boreholes (Liu et al., 2016) and could be used to update the propagation velocity model, as suggested elsewhere in the literature (Ravasi et al., 2015b). When the multidimensional Marchenko equation is used to retrieve the wavefields at the lower array, such velocity updates seem impossible, as confirmed by Figure 6c and 6d, where kinematic variations cannot be observed.

Linear or nonlinear imaging?

By single-sided redatuming from above (i.e., inversion of equation 14), one can separate all reflections that occur below a specified boundary from all orders of interaction with the part of the medium above that boundary. This kind of redatuming has proven useful to eliminate multiple reflections from the shallow subsurface that can interfere with primary (and multiple) reflections from deeper targets (Wapenaar and van der Neut, 2010; Ravasi et al., 2015a). Hence, this approach is relevant for linear and nonlinear imaging of a target volume that is buried below strong shallow heterogeneities. Equivalently, one can separate all reflections that occur above a specified boundary from all orders of interaction below that boundary by single-sided redatuming from below (i.e., inversion of equation 23) (Ravasi et al., 2016). This strategy can be used to eliminate reflections from below a target volume, for instance, deep salt body reflections in seismic imaging (Jones and Davison, 2014) or the chest wall reflection in ultrasonic breast imaging (Ozmen et al., 2015). Because reflections from below the volume arrive after the latest possible primary reflections from inside the volume (whose traveltimes can be directly computed from the macro model), the primary reflections from inside the volume can also be isolated from deeper reflections by truncating the reflection records in time. Hence, single-sided redatuming from below has limited applications for linear imaging processes, which rely on primary reflections only. However, truncation is insufficient to isolate multiple reflections inside the volume that may interfere with (primary and multiple) reflections from below the volume. Therefore, single-sided redatuming from below seems especially relevant if multiple reflections are included in the retrieved response, which is important to image nonlinearity inside the target volume. Similar statements can be made about target-enclosed redatuming. If linear imaging inside a target volume is our objective, the target-enclosed scheme offers little benefits over single-sided redatuming from above with the relevant truncations. However, if we strive for nonlinear imaging, the developed methodology offers the potential to separate all orders of reflections inside the volume from the interactions with other parts of the medium.

By retrieving target-enclosed extended images, the original data set, which is recorded in infinite space, can be transformed into a smaller virtual data set. Because the virtual data are dependent on the medium parameters of a limited, finite volume only, it is speculated that the computational costs of local inversion for the medium properties inside the target volume can be reduced significantly. Besides virtual reflection responses, we also retrieve virtual transmission responses of the target volume. As we have demonstrated in Figure 8b, the retrieved reflection and transmission responses can be combined to evaluate novel imaging conditions that rely on closed boundary representations (Ravasi et al., 2014), leading to superior seismic resolution. To benefit from these, it is crucial that multiple reflections are included in the redatumed responses, which we have achieved by solving the inverse problems derived herein.

CONCLUSION

We have derived two inversion schemes to retrieve target-enclosed extended images. The first scheme requires as input a set of Green's functions with sources at a single acquisition boundary at the earth's surface and receivers at two boundaries in the subsurface, selected above and below a specified target volume. These Green's functions can either be recorded, modeled, or computed from the multidimensional Marchenko equation. The second scheme requires focusing functions (which are also obtained from the multidimensional Marchenko equation) with focal points at the acquisition boundary and receivers at the two target-enclosing boundaries. The output of both schemes consists of (1) a reflection response at the upper boundary from above, (2) a reflection response at the lower boundary from below, and (3) the transmission response of the target volume.

The redatumed data can be used to image the target volume from above or from below. If the redatuming input is computed with the multidimensional Marchenko equation, it can be shown that both redatuming schemes are based on the same equations and are independent on the part of the medium below the target volume. In this case, the images from above and below are similar. If the redatuming input is measured (for instance, by boreholes in the subsurface), it is speculated that reflections from below the target may enhance illumination and consequently improve the resolution. In this case, the images from below and above are different, given that the velocity model that is used for imaging is inaccurate. This offers opportunities for updating the velocity model in cases where physical receivers are deployed inside the subsurface. We emphasize that such updates are not possible if the redatuming input is computed from the multidimensional Marchenko equation.

The redatumed data contain all linear and nonlinear interactions inside the target volume but excludes all interactions from outside. Hence, these data can be valuable input to invert for medium properties in a specified target volume. Because the redatumed data depend on a limited number of medium parameters only, the computational burden of "local" inversion is expected to be significantly less than the burden of an equivalent "global" inverse problem. As we have transformed single-sided reflection data into virtual data with sources and receivers at two enclosing boundaries, the redatumed data can also be used to evaluate novel imaging conditions that are derived from closed-boundary representations. We have shown that seismic images with superior resolution can be generated in this way (compared with the results of linear imaging). We emphasize that the generation of such images is only possible if an accurate model of the target volume is available.

ACKNOWLEDGMENTS

J. van der Neut thanks the Nederlandse Organisatie voor Wetenschappelijk Onderzoek, domein Toegepaste Technische Wetenschappen (STW/TTW) (grant no. VENI.13078) for financially supporting his research. M. Ravasi thanks the Edinburgh Interferometry Project sponsors (ConocoPhillips, Schlumberger Gould Research, Statoil, and Total) for supporting his research. Part of this research was conducted during an exchange of J. van der Neut at the University of Edinburgh. We thank A. Curtis, G. Meles, S. de Ridder, and C. da Costa Filho (University of Edinburgh) for enabling this exchange and for fruitful discussions that have contributed significantly to this paper. Another part has been conducted at NTNU Trondheim, where we appreciated B. Arntsen for hosting. Finally, we acknowledge K. Wapenaar, E. Slob, J. Thorbecke, M. Staring, L. Zhang, C. Reinicke, and J. Brackenhoff from the Delft University of Technology for their collaboration.

APPENDIX A

DISCRETIZED SQUARE-ROOT OPERATOR

In this appendix, we discuss how the square-root operator $\mathcal{H}_1$ can be computed numerically. We consider an arbitrary wavefield $\mathbf{p}_k$ at a depth level $\partial\mathcal{V}_k$ (with $k=i$ or $k=j$) at a particular frequency, which is discretized as a column vector, where each sample represents a spatial location. The (modified) Helmholtz operator $\mathcal{H}_2$ at level $\partial\mathcal{V}_k$ is discretized as matrix $\mathbf{H}_{2k}$, which acts at the wavefield, according to $\mathbf{H}_{2k}\mathbf{p}_k$. The required matrix can be obtained by discretizing equation 2 as

$$\mathbf{H}_{2k} = \omega^2\mathbf{C}_k^{-2} + \mathbf{P}_k\Delta\mathbf{P}_k^{-1}\Delta, \tag{A-1}$$

where $\mathbf{C}_k$ and $\mathbf{P}_k$ are the diagonal matrices with velocities and densities at $\partial\mathcal{V}_k$, respectively, which we assume to be (approximately) known at the redatuming boundaries. Further, Δ is a first-order finite-difference operator. The square-root operator $\mathbf{H}_{1k}$ can be computed by eigenvalue decomposition of matrix $\mathbf{H}_{2k}$ (Grimbergen et al., 1998), according to $\mathbf{H}_{2k}=\mathbf{L}_k\mathbf{\Lambda}_k\mathbf{L}_k^{-1}$, where $\mathbf{\Lambda}_k$ is a diagonal matrix with eigenvalues and $\mathbf{L}_k$ is a matrix with eigenvectors. The square-root operator is obtained by taking the square roots of the eigenvalues and recomputing the matrix: $\mathbf{H}_{1k}=\mathbf{L}_k\mathbf{\Lambda}_k^{1/2}\mathbf{L}_k^{-1}$. In a similar way, the inverse of the square-root operator can be computed as $\mathbf{H}_{1k}^{-1}=\mathbf{L}_k\mathbf{\Lambda}_k^{-1/2}\mathbf{L}_k^{-1}$. Akin to the discretized Helmholtz operator, the discretized square-root operator and its inverse can be applied directly to the wavefield $\mathbf{p}_k$, according to $\mathbf{H}_{1k}\mathbf{p}_k$ and $\mathbf{H}_{1k}^{-1}\mathbf{p}_k$.

APPENDIX B

FREQUENCY-DOMAIN IMPLEMENTATION

In this appendix, we show how the matrices $\mathbf{A}(x_{ka}^{\pm})$ (with $x=G$ or $x=f$, and $k=i$ or $k=j$) that appear in this paper can be computed in practice for an arbitrary wavefield $x_{ka}^{\pm}$. Here, we assume that all equations are evaluated in the frequency domain at a particular frequency ω. For equivalent representations in the time domain, see Appendix C. By comparing equations 13 and 14 (with $x_{ka}^{\pm}=G_{ia}^{+}$), it is not hard to see that matrix $\mathbf{A}(x_{ka}^{\pm})$ can be written as

$$\mathbf{A}(x_{ka}^{\pm}) = \frac{2}{\omega}\mathbf{P}_k^{-1}\mathbf{M}(x_{ka}^{\pm})\mathbf{H}_{1k}, \tag{B-1}$$

where $\mathbf{M}(x_{ka}^{\pm})$ is a matrix for multidimensional convolution with the wavefield $x_{ka}^{\pm}$, $\mathbf{H}_{1k}$ is the discretized square-root operator (see Appendix A), and $\mathbf{P}_k^{-1}$ is a block-diagonal matrix with the inverse densities (all quantities are evaluated with properties along boundary $\partial\mathcal{V}_k$). Equation B-1 can also be applied to compute all other matrices $\mathbf{A}(x_{ka}^{\pm})$ in this paper.

APPENDIX C

TIME-DOMAIN IMPLEMENTATION

To construct a matrix $\mathbf{A}(x_{ka}^{\pm})$ for multidimensional convolution with an arbitrary wavefield $x_{ka}^{\pm}$ in the time domain, we modify equation B-1 in the following way:

$$\mathbf{A}(x_{ka}^{\pm}) = \mathbf{F}_o^{-1}\mathbf{B}(2\omega^{-1}\mathbf{P}_k^{-1}\mathbf{M}(x_{ka}^{\pm})\mathbf{H}_{1k})\mathbf{F}_o\mathbf{\Upsilon}_H, \tag{C-1}$$

where $\mathbf{F}_o$ is a matrix for temporal Fourier transformation and $\mathbf{F}_o^{-1}$ is its inverse. Furthermore, we have defined $\mathbf{B}(\mathbf{Y}(\omega))$ to compute a block-diagonal matrix, where each block contains matrix $\mathbf{Y}(\omega)=2\omega^{-1}\mathbf{P}_k^{-1}\mathbf{M}(x_{ka}^{\pm})\mathbf{H}_{1k}$ at the corresponding frequency ω. Unlike equation B-1, which can be applied to an individual frequency slice, our formulation in the time domain requires that all time samples are considered. However, this formulation allows us to enforce that the solution is causal. In equation C-1, we have done so by including matrix $\mathbf{\Upsilon}_H$, which passes only causal entries.

REFERENCES

Aldawood, A., I. Hoteit, G. Turkiyyah, and T. Alkhalifah, 2015, Analysing the effects of least-squares datuming on VSP multiple imaging: 77th Annual International Conference and Exhibition, EAGE, Extended Abstracts, P212.

Amundsen, L., 2001, Elimination of free-surface related multiples without need of the source wavelet: Geophysics, **66**, 327–341, doi: 10.1190/1.1444912.

Bakulin, A., and R. Calvert, 2006, The virtual source method: Theory and case study: Geophysics, **71**, no. 4, SI139–SI150, doi: 10.1190/1.2216190.

Behura, J., K. Wapenaar, and R. Snieder, 2014, Autofocus imaging: Image reconstruction based on inverse scattering theory: Geophysics, **79**, no. 3, A19–A26, doi: 10.1190/geo2013-0398.1.

Berkhout, A. J., 1980, Seismic migration: Imaging of acoustic energy by wavefield extrapolation: Elsevier Science Pub. Co.

Berryhill, J. R., 1984, Wave-equation datuming before stack: Geophysics, **49**, 2064–2066, doi: 10.1190/1.1441620.

Broggini, F., R. Snieder, and K. Wapenaar, 2012, Focusing the wavefield inside an unknown 1D medium: Beyond seismic interferometry: Geophysics, **77**, no. 5, A25–A28, doi: 10.1190/geo2012-0060.1.

Broggini, F., R. Snieder, and K. Wapenaar, 2014, Data-driven wavefield focusing and imaging with multidimensional deconvolution: Numerical examples for reflection data with internal multiples: Geophysics, **79**, no. 3, WA107–WA115, doi: 10.1190/geo2013-0307.1.

Byun, J., J. Yu, and S. J. Seol, 2010, Crosswell monitoring using virtual sources and horizontal wells: Geophysics, **75**, no. 3, SA37–SA43, doi: 10.1190/1.3427175.

Claerbout, J. F., 1971, Toward a unified theory of reflector mapping: Geophysics, **36**, 467–481, doi: 10.1190/1.1440185.

da Costa Filho, C., G. Meles, and A. Curtis, 2017, Elastic internal multiple analysis and attenuation using Marchenko and interferometric methods: Geophysics, **82**, no. 2, Q1–Q12, doi: 10.1190/geo2016-0162.1.

da Costa Filho, C. A., M. Ravasi, and A. Curtis, 2015, Elastic P and S wave autofocus imaging with primaries and internal multiples: Geophysics, **80**, no. 5, S187–S202, doi: 10.1190/geo2014-0512.1.

Davydenko, M., and D. J. Verschuur, 2016, Full-wavefield migration: Using surface and internal multiples in imaging: Geophysical Prospecting, **65**, 7–21, doi: 10.1111/1365-2478.12360.

de Bruin, C. G. M., C. P. A. Wapenaar, and A. J. Berkhout, 1990, Angle-dependent reflectivity by means of prestack migration: Geophysics, **55**, 1223–1234, doi: 10.1190/1.1442938.

Fleury, C., and I. Vasconcelos, 2012, Imaging condition for nonlinear scattering-based imaging: Estimate of power loss in scattering: Geophysics, **77**, no. 1, S1–S18, doi: 10.1190/geo2011-0135.1.

Grimbergen, J. L. T., F. J. Dessing, and K. Wapenaar, 1998, Modal expansion of one-way operators in laterally varying media: Geophysics, **63**, 995–1005, doi: 10.1190/1.1444410.

Halliday, D., and A. Curtis, 2010, An interferometric theory of source-receiver scattering and imaging: Geophysics, **75**, no. 6, SA95–SA103, doi: 10.1190/1.3486453.

Jones, I. F., and I. Davison, 2014, Seismic imaging in and around salt bodies: Interpretation, **2**, no. 4, SL1–SL20, doi: 10.1190/INT-2014-0033.1.

Lin, T. T., and F. J. Herrmann, 2013, Robust estimation of primaries by sparse inversion via one-norm minimization: Geophysics, **78**, no. 3, R133–R150, doi: 10.1190/geo2012-0097.1.

Lin, T. Y., and F. J. Herrmann, 2016, Estimation of primaries by sparse inversion with scattering-based multiple predictions for data with large gaps: Geophysics, **81**, no. 3, V183–V197, doi: 10.1190/geo2015-0263.1.

Liu, Y., J. van der Neut, B. Arntsen, and K. Wapenaar, 2016, Combination of surface and borehole seismic data for robust target-oriented imaging: Geophysical Journal International, **205**, 758–776.

Malcolm, A. E., M. V. de Hoop, and H. Calandra, 2007, Identification of image artifacts from internal multiples: Geophysics, **72**, no. 2, SI123–SI132, doi: 10.1190/1.2434780.

Malcolm, A. E., B. Ursin, and M. V. de Hoop, 2009, Seismic imaging and illumination with internal multiples: Geophysical Journal International, **176**, 847–864, doi: 10.1111/j.1365-246X.2008.03992.

Mehta, K., A. Bakulin, J. Sheiman, R. Calvert, and R. Snieder, 2007, Improving the virtual source method by wavefield separation: Geophysics, **72**, no. 4, V79–V86, doi: 10.1190/1.2733020.

Meles, G., K. Löer, M. Ravasi, A. Curtis, and C. A. da Costa Filho, 2015, Internal multiple prediction and removal using Marchenko autofocusing and seismic interferometry: Geophysics, **77**, no. 5, S1–S18.

Meles, G., K. Wapenaar, and A. Curtis, 2016, Reconstructing the primary reactions in seismic data by Marchenko redatuming and convolutional interferometry: Geophysics, **81**, no. 2, Q15–Q26, doi: 10.1190/geo2015-0377.1.

Mildner, C., F. Broggini, J. O. A. Robertsson, D.-J. van Manen, and S. Greenhalgh, 2017, Target-oriented velocity analysis using Marchenko-redatumed data: Geophysics, **82**, no. 2, R75–R86, doi: 10.1190/geo2016-0280.1.

Ordoñez, A., W. Söllner, T. Klüver, and L. J. Gelius, 2016, Subsurface reflectivity estimation from imaging of primaries and multiples using amplitude-normalized separated wavefields: Geophysics, **81**, no. 3, S101–S117, doi: 10.1190/geo2015-0385.1.

Ozmen, N., R. Dapp, M. Zapf, H. Gemmek, N. V. Ruiter, and K. W. van Dongen, 2015, Comparing different ultrasound imaging methods for breast cancer detection: IEEE Transactions on Ultrasonics Ferroelectrics, and Frequency Control, **62**, 637–646, doi: 10.1109/TUFFC.2014.006707.

Paffenholz, J., B. McLain, J. Zaske, and P. Keliher, 2002, Subsalt multiple attenuation and imaging: Observations from the Sigsbee2B synthetic data set: 72nd Annual International Meeting, SEG, Expanded Abstracts, 2122–2125.

Paige, C. C., and M. A. Saunders, 1982, LSQR: An algorithm for sparse linear equations and sparse least squares: ACM Transactions on Mathematical Software, **8**, 43–71, doi: 10.1145/355984.355989.

Ravasi, M., G. Meles, A. Curtis, Z. Rawlinson, and Y. Liu, 2015a, Seismic interferometry by multi-dimensional deconvolution without wavefield separation: Geophysical Journal International, **202**, 1–16, doi: 10.1093/gji/ggv062.

Ravasi, M., I. Vasconcelos, and A. Curtis, 2014, Beyond conventional migration: Nonlinear elastic subsalt imaging with transmissions and two-sided illumination: Geophysical Journal International, **198**, 1173–1185, doi: 10.1093/gji/ggu192.

Ravasi, M., I. Vasconcelos, A. Curtis, and G. Meles, 2015b, Elastic extended images and velocity-sensitive objective functions using multiple reflections and transmissions: Geophysical Journal International, **202**, 943–960, doi: 10.1093/gji/ggv173.

Ravasi, M., I. Vasconcelos, A. Kritski, A. Curtis, C. A. da Costa Filho, and G. A. Meles, 2016, Target-oriented Marchenko imaging of a North Sea field: Geophysical Journal International, **205**, 99–104, doi: 10.1093/gji/ggv528.

Sava, P., and I. Vasconcelos, 2010, Extended imaging conditions for wave-equation migration: Geophysical Prospecting, **59**, 35–55, doi: 10.1111/j.1365-2478.2010.00888.

Schuster, G. T., and M. Zhou, 2006, A theoretical overview of model-based and correlation based redatuming methods: Geophysics, **71**, no. 4, SI103–SI110, doi: 10.1190/1.2208967.

Schuster, J., 2009, Seismic interferometry: Cambridge Press.

Singh, S., and R. Snieder, 2017, Source-receiver Marchenko redatuming: Obtaining virtual receivers and virtual sources in the subsurface: Geophysics, **82**, no. 3, Q13–Q21, doi: 10.1190/geo2016-0074.1.

Singh, S., R. Snieder, J. Behura, J. van der Neut, K. Wapenaar, and E. Slob, 2015, Marchenko imaging: Imaging with primaries, internal multiples, and free-surface multiples: Geophysics, **80**, no. 5, S165–S174, doi: 10.1190/geo2014-0494.1.

Slob, E., K. Wapenaar, F. Broggini, and R. Snieder, 2014, Seismic reflector imaging using internal multiples with Marchenko-type equations: Geophysics, **79**, no. 2, S63–S76, doi: 10.1190/geo2013-0095.1.

Snieder, R., K. Wapenaar, and K. Larner, 2006, Spurious multiples in seismic interferometry of primaries: Geophysics, **71**, no. 4, SI111–SI124, doi: 10.1190/1.2211507.

Thomson, C. P., P. Kitchenside, and R. Fletcher, 2016, Theory of reflectivity blurring in seismic depth imaging: Geophysical Journal International, **205**, 837–855, doi: 10.1093/gji/ggw025.

Tu, N., and F. J. Herrmann, 2015, Fast imaging with surface-related multiples by sparse inversion: Geophysical Journal International, **201**, 304–317, doi: 10.1093/gji/ggv020.

Valenciano, A., and N. Chemingui, 2015, Introduction to this special section: Multiples from attenuation to imaging: The Leading Edge, **34**, 742–742, doi: 10.1190/tle34070742.1.

van Borselen, R. G., J. T. Fokkema, and P. M. van den Berg, 1996, Removal of surface related wave phenomena — The marine case: Geophysics, **61**, 202–210, doi: 10.1190/1.1443940.

van der Neut, J., D. Alexandrov, and A. Bakulin, 2016, Shallow virtual source redatuming by multi-dimensional deconvolution: Geophysical Prospecting, **64**, 4–18, doi: 10.1111/1365-2478.12258.

van der Neut, J., E. Slob, K. Wapenaar, J. Thorbecke, R. Snieder, and F. Broggini, 2013, Interferometric redatuming of autofocused primaries and internal multiples: 83rd Annual International Meeting, SEG, Expanded Abstracts, 4589–4594.

van der Neut, J., I. Vasconcelos, and K. Wapenaar, 2015, On Green's function retrieval by iterative substitution of the coupled Marchenko equations: Geophysical Journal International, **203**, 792–813, doi: 10.1093/gji/ggv330.

van der Neut, J., and K. Wapenaar, 2016, Adaptive overburden elimination with the multidimensional Marchenko equation: Geophysics, **81**, no. 5, T265–T284, doi: 10.1190/geo2016-0024.1.

van Groenestijn, G. H. A., and D. J. Verschuur, 2009, Estimating primaries by sparse inversion and application to near-offset data reconstruction: Geophysics, **74**, no. 3, A23–A28, doi: 10.1190/1.3111115.

Vasconcelos, I., and J. Rickett, 2013, Broadband extended images from joint inversion of multiple blended wavefields: Geophysics, **78**, no. 2, WA147–WA158, doi: 10.1190/geo2012-0475.1.

Vasconcelos, I., P. Sava, and H. Douma, 2010, Nonlinear extended images via image-domain interferometry: Geophysics, **75**, no. 6, SA105–SA115, doi: 10.1190/1.3494083.

Vasconcelos, I., K. Wapenaar, J. van der Neut, C. Thomson, and M. Ravasi, 2015, Using inverse transmission matrices for Marchenko redatuming in highly complex media: 85th Annual International Meeting, SEG, Expanded Abstracts, 5081–5086.

Wapenaar, C. P. A., and J. L. T. Grimbergen, 1996, Reciprocity theorems for one-way wavefields: Geophysical Journal International, **127**, 167–177.

Wapenaar, K., J. Thorbecke, J. van der Neut, F. Broggini, E. Slob, and R. Snieder, 2014, Marchenko imaging: Geophysics, **80**, no. 5, S165–S174.

Wapenaar, K., and J. van der Neut, 2010, A representation for Green's function retrieval by multidimensional deconvolution: Journal of the Acoustical Society of America, **128**, EL366–EL371, doi: 10.1121/1.3509797.

Wapenaar, K., J. van der Neut, and E. Slob, 2017, On the role of multiple in Marchenko imaging: Geophysics, **82**, no. 3, A1–A5, doi: 10.1190/geo2016-0323.1.

Weglein, A. B., F. V. Araújo, P. M. Carvalho, R. H. Stolt, K. H. Matson, R. T. Coates, D. Corrigan, D. J. Foster, S. A. Shaw, and H. Zhang, 2003, Inverse scattering series and seismic exploration: Inverse Problems, **19**, R27–R83, doi: 10.1088/0266-5611/19/6/R01.

Xue, Y., and G. T. Schuster, 2008, Least squares datuming with the wave equation: 78th Annual International Meeting, SEG, Expanded Abstracts, 2366–2370.

Youn, O. K., and H. Zhou, 2001, Depth imaging with multiples: Geophysics, **66**, 246–255, doi: 10.1190/1.1444901.